same land use/cover according to "seasonal" dynamics, almost similar weather/climatic conditions) automatically allows the overcoming of possible site effects [22]. For instance, any signal variation related to terrain shadows, which should be almost constant considering imagery acquired always in the same month of the year at the same time, is inherently taken into account by the proposed method. Furthermore, signal fluctuations due to spurious/random effects (sun glint contamination, suspended sediment variability, etc.) can only determine a higher standard deviation, thus resulting in a reduction of the ALICE index values and a much more selective identification of anomalous events [49,50]. As assessed by an independent work focused on RST [51], the investigated satellite historical series should consist of about 80 images to guarantee representative background signal. Such a number, considering a monthly temporal window and a sensor offering a daily temporal resolution, roughly corresponds to a 3-year long time series, representing indeed the minimum time span for a reliable RST implementation.

During the generation of the reference fields, as well as during the change detection step, cloudy pixels were identified and discarded from the detection step implementing the One Channel Algorithm (OCA) method [52,53]. Such an approach, still based on the RST prescriptions, analyses historical series of VIIRS I3 and I5 data to identify clouds as statistically high reflectivity or low temperature objects. Concerning cloud shadows, a specific algorithm based on ALICE indices (described in the next section) has been developed and tested here for the first time, to ensure a reliable identification of flooded area by optical data.

In its previous application to flooded area detection (e.g., [22,23]) RST-FLOOD used the ratio and/or the difference between the signals measured in the RED and NIR channels (i.e., RED/NIR and/or RED-NIR) of AVHRR (channel 1: 0.58–0.68 µm and channel 2: 0.725–1.00 µm, both at 1 km of spatial resolution) and MODIS (channel 1: 0.62–0.67 µm and channel 2: 0.841–0.876 µm, both a t 250 m of spatial resolution) as the reference signal (i.e., $V(x,y,t)$ in Equation (1)). In particular, the ratio index demonstrated to be more robust respect to false positives, while the difference RED-NIR resulted more sensitive to the presence of flooded area [23].

Concerning VIIRS Imagery data, in addition to the indexes above defined [14], flooded area can be detected in different single bands and/or exploiting their combination, due to the specific spectral response of water in the VNIR region [6,11,54]. To better highlight such a behaviour within the local-scale conditions, the spectral profile for different signals along the red transect shown in Figure 1, has been investigated (Figure 6). Reflectance in both single (i.e., RED, NIR and SWIR, Figure 6a) and combined (i.e., RED − SWIR, RED/SWIR, NDSI-Normalized Difference Snow Index, Figure 6b) VIIRS I-bands were analysed.

Considering the reflectance trends along the selected transect at wavelengths between 0.6 µm and 1.64 µm (Figure 6a), a clear signal change is observable in correspondence of the areas perturbed by the water presence. In detail, the presence of turbid waters (i.e., rich in sediment) causes an I1 signal increase that is no more detectable in the two channels at higher wavelength, where the water absorption properties produce a signal decrease. The relative variation between probably flooded/no-flooded area is relatively higher for I3 channel (77%) than I2 one (57%), suggesting better sensitivity of I3 towards these features. According to these outcomes, within the band combination analysis (Figure 6b), we did not consider the NIR (I2) channel anymore. Plots shown in Figure 5b highlight the good sensitivity of the signal band combinations (i.e., I1–I3 or I1/I3) for flooded area detection, with the ratio providing the best score in terms of signal variation. In addition, also their combination in terms of normalized difference, namely the NDSI (NDSI = RED − SWIR/RED + SWIR [55]), proves to be an index suitable for water detection purposes [56] thanks to the high water reflectance contrast at these two wavelengths [11,15].

On the basis of the above discussed analysis, the ALICE index (Equation (1)) was preliminarily computed on the following five signals: I1, I3, I1 − I3, I1/I3 and NDSI = (I1 − I3/I1 + I3), in order to select the best suitable metric (single band or combination) for flooded area detection, in terms of both

reliability and sensitivity. It is worth noting that only the ALICE$_{SWIR}$ index should show low negative values in presence of flooded area, while, for all the others, high positive values have to be expected.
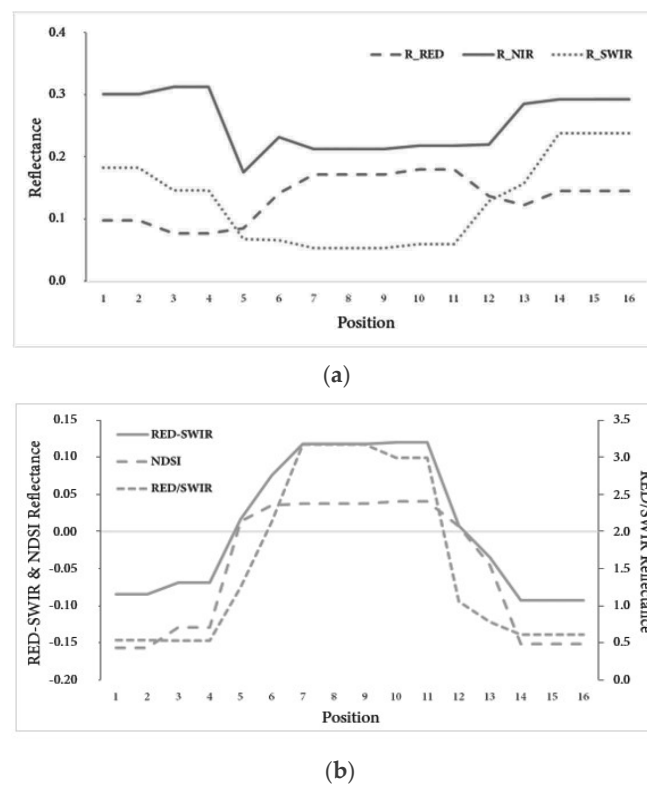

(**a**)

(**b**)

Figure 6. Reflectance variability profile along the red segment shown in Figure 1 for: (**a**) RED (I1), NIR (I2), SWIR (I3) VIIRS I-bands of 04/12/2013 at 12.10 GMT and the combinations (**b**) RED − SWIR, RED/SWIR, NDSI = (RED − SWIR)/(RED + SWIR).

3.4. Cloud Shadows Removal

In this study, we investigated, for the first time, the potential of the RST approach to identifying cloud shadows, using the VIIRS I-bands. It is worth pointing out that, to our knowledge, this is the first attempt to exploit these data to detect cloud shadows. The current cloud mask algorithm for VIIRS I-Band indeed does not contain any confidence flag for shadows [57]. It is also important to specify that the approach we are proposing is based on a preliminary version, implemented for identifying (and removing before further analyses) clouds shadows (just for clouds on land). The performances it offers using the developed criterion, shown in this paper, refers exclusively to the flood analysed in this work. Other tests on wider regions are needed to confirm its feasibility and make it working well for all situations. In this first approach, the algorithm does not use geometry-based information (e.g., view angle of the satellite sensor, the solar zenith angle, the solar azimuth angle and the relative height of the cloud) to assess the cloud shadow location. In any case, it is worth mentioning that an assessment of the reliability of the RST-based cloud shadow product is beyond the scope of this paper and will be object of future works.

Cloud shadows can be considered, from a statistical point of view, as anomalous signals randomly perturbing the investigated signal at pixel level for the considered scene. Therefore, they can be analysed by implementing the RST approach selecting spectral radiances most sensitive to their presence [58], namely the reflectance values measured in the I1, I2 and I3 VIIRS bands. [58] showed the difference of reflectance values between clear pixels and cloud shadow contaminated pixels on vegetation, settlement and water bodies are shown, for the Landsat 8 bands (from Blue to SWIR). They found that NIR and SWIR bands have the biggest difference in average between clear pixels and cloud

shadow contaminated pixels. Despite this, the choice of the most suitable metric (e.g. between the single or a bands combination) is not trivial, as shadows show a spectral response in the VIS-SWIR spectral range almost similar to those of flooded area [59]. Investigating the differences in values of the ALICE indices (i.e., $ALICE_{RED}$, $ALICE_{NIR}$ and $ALICE_{SWIR}$) for shadows and flooded area, it is worth considering that:

- in the RED (I1), flooded pixels should show higher values of $ALICE_{RED}$ than the shadow-affected ones, due to their relative increase in reflectance at this wavelength;
- in the NIR (I2) and SWIR (I3), both flooded and shadow pixels show low (negative) values of $ALICE_{NIR}$ and $ALICE_{SWIR}$.

Therefore, a combination of those signals can allow a quite reliable identification of cloud shadows, which were mapped using the following rule:

$$\text{if } [ALICE_{RED} < -2 \text{ and } ALICE_{NIR} < -2 \text{ and } ALICE_{SWIR} < -2] \text{ then "shadow"}$$

where the value "-2" used for all ALICE indices is the minimum level assuring the statistical significance of detected pixels. Besides, a 1.5 km - buffer zone around each potential cloud shadow affected pixel has been applied, to compensate for missed detections.

For its inherent construction, such a criterion, applied only on cloud-free pixels, looks for those areas concurrently showing a statistically significant decrease in the signal acquired in the first three VIIRS Imagery bands. Therefore, apart from a few spurious and random signals, it should allow at discriminating flooded area from cloud shadows.

4. Results

4.1. Cloud Shadow

The cloud and shadow masks produced by the approach above mentioned are shown in Figure 7 and refer to the most two cloudy (on land) images (i.e., 05/12/2013 at 11:52 GMT and 07/12/2013 at 11:12 GMT, see Figure 5b,d) among the ones analysed in this paper. Furthermore, for each of them, also the corresponding VIIRS RGB false colour image is plotted.
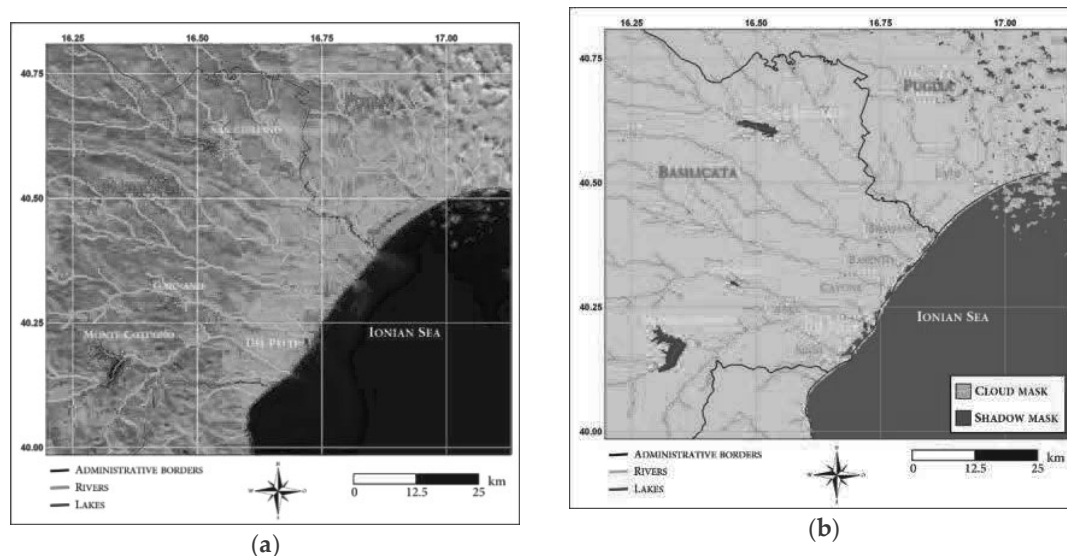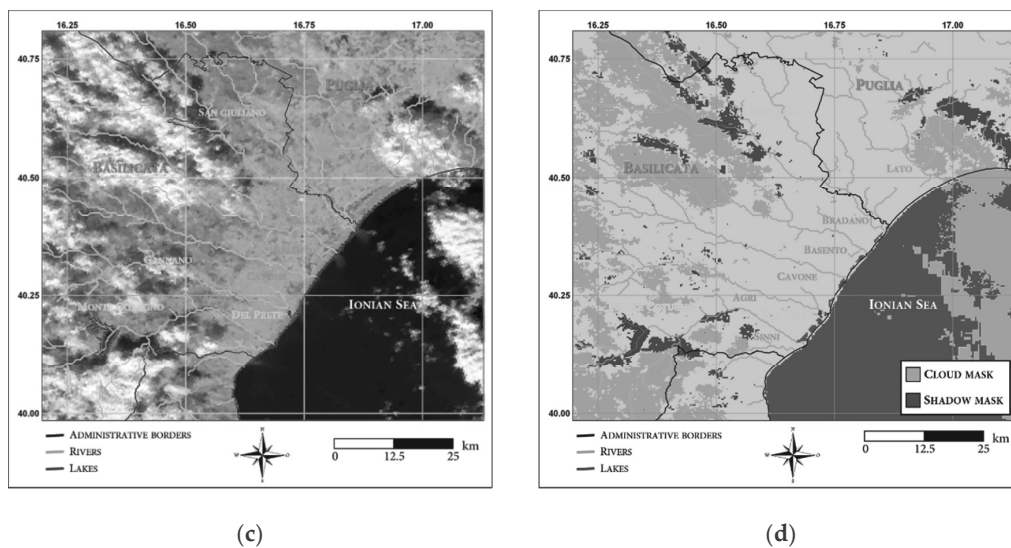

Figure 7. *Cont.*

(c)　　　　　　　　　　　　　　　　　　　　　　　(d)

Figure 7. (**a**) RGB False Colour (R = SWIR, G = NIR, B = RED) of VIIRS Imagery data acquired on 5 December 2013 at 11:52 GMT; (**b**) cloud and shadow masks for the image shown in (**a**); (**c**) RGB False Colour (R = SWIR, G = NIR, B = RED of VIIRS Imagery data acquired on 7 December 2013 at 11:12 GMT; (**d**) cloud and shadow masks for the image shown in (**c**).

The maps in Figure 7b,d seem to indicate the good potential of this preliminary RST-based indicator in detecting anomalous pixels likely affected by cloud shadows. The visual comparison to the VNG outputs (see Figure 5b,d) also indicates a general agreement between the two products, even if a straight inter-comparison is not possible, because of the different cloud detection strategy adopted. Obviously, at the current state, residual cloud shadows not properly identified will expose RST-FLOOD to possible false positive detection.

4.2. Selection of the Most Suitable VIIRS RST-FLOOD Indicator

As already mentioned, the first almost cloudy-free VIIRS daytime image acquired over the area under investigation soon after the event was on 4 December 2013 at 12:10 GMT, shown in RGB False Colour (R = I3, G = I2, B = I1) in Figure 1. This image has been selected as benchmark for assessing ALICE indices performances (Figure 8), being the one temporally closest to the flood peak. In each of the five maps reported in Figure 8, pixels showing statistically significant (i.e., higher/lower than |3|) ALICE values have been depicted in red.

The results based on the $ALICE_{RED}$ index (Figure 8a) highlighted its poor reliability in discriminating flooded pixels. Although several pixels are located along the main rivers in the area, there are indeed more others randomly spread out all over the ROI. These effects disappear in all the other maps, whose analysis seems to suggest a quite similar behaviour for the other four indices.

Hence, excluding the $ALICE_{RED}$ index (Figure 8a), the number of flooded pixels identified all over the scene by each of the other indices has been summarized in Table 2, in which also the mean and maximum ALICE values are reported. The same information has been listed for anomalous pixels detected along the Basento River.

The $ALICE_{SWIR}$ appears as the most conservative index in identifying anomalous pixels, compared with the others (see Table 2). An in-depth investigation of anomalies discriminated by all the other indices suggests the following considerations. The ALICE index, when using the RED and SWIR reflectances, combined as difference, ratio and normalized difference, overall provide the same information on flooded area extent, flagging as anomalous a very similar number of pixels (see Table 2). In particular, among them, the $ALICE_{RED-SWIR}$ and $ALICE_{RED/SWIR}$, unlike the $ALICE_{NDSI}$, seem more exposed to the detection of anomalous/spurious pixels along the coastline. Accordingly, the $ALICE_{NDSI}$ appears as the most performing index, offering the best trade-off between sensitivity and reliability.
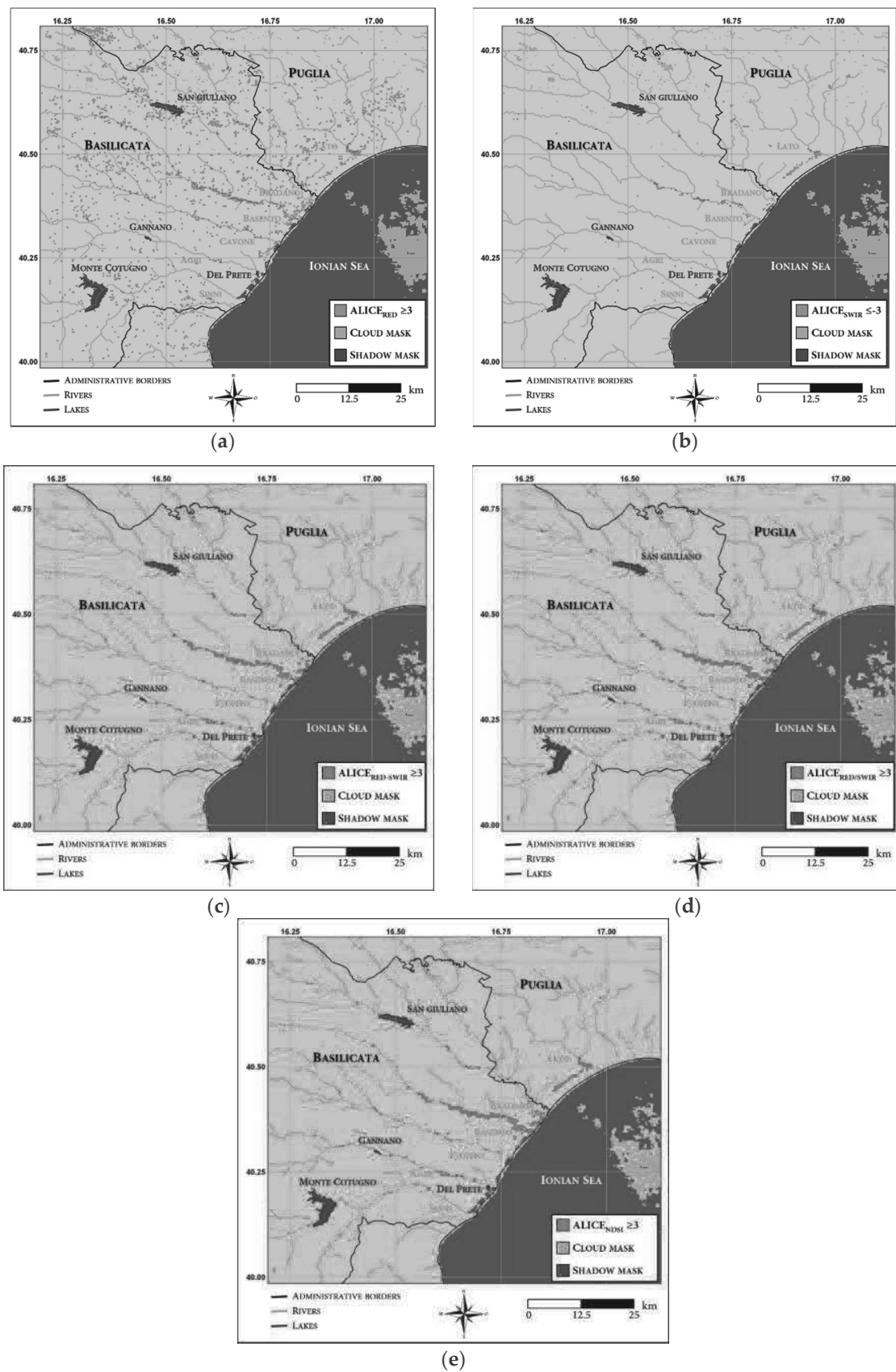
Figure 8. Anomalous pixels detected by: (**a**) ALICE$_{RED}$, (**b**) ALICE$_{SWIR}$, (**c**) ALICE$_{RED-SWIR}$, (**d**) ALICE$_{RED-SWIR}$, (**e**) ALICE$_{NDSI}$ on 04/12/2013 at 12:10 GMT.

Table 2. Statistics of the ALICE indices all over the scene and for anomalous pixels along Basento River.

ALICE Index	All Scene			Basento River		
	# Anomalous Pixels	Mean	Max/Min	# Anomalous Pixels	Mean	Max/Min
ALICE$_{SWIR}$	220	−2.42	−28.16	71	−3.98	−7.48
ALICE$_{RED-SWIR}$	604	4.70	17.15	230	6.28	17.15
ALICE$_{RED/SWIR}$	679	8.92	61.83	247	3.06	61.83
ALICE$_{NDSI}$	638	5.78	23.74	256	3.01	23.74

The analysis for the Basento River shows almost similar outcomes respect to the whole scene in terms of detected ALICE values but with the ALICE$_{NDSI}$ identifying the largest number of anomalous pixels (i.e., 256). Therefore, on the basis of the above discussed results, the ALICE$_{NDSI}$ has been selected as the benchmark index in the next analyses, resulting less affected by suspended sediments and showing a good sensitivity in detecting flooded area.

A map of the detected anomalous areas for the VIIRS image of 4 December 2013 is plotted in Figure 9 where different colours (from red to yellow) indicate increasing significance levels of the ALICE$_{NDSI}$ index. The pixels detected as anomalous at the highest ALICE$_{NDSI}$ (i.e., the yellow ones) are representative of local conditions extremely different from those expected in the ROI.
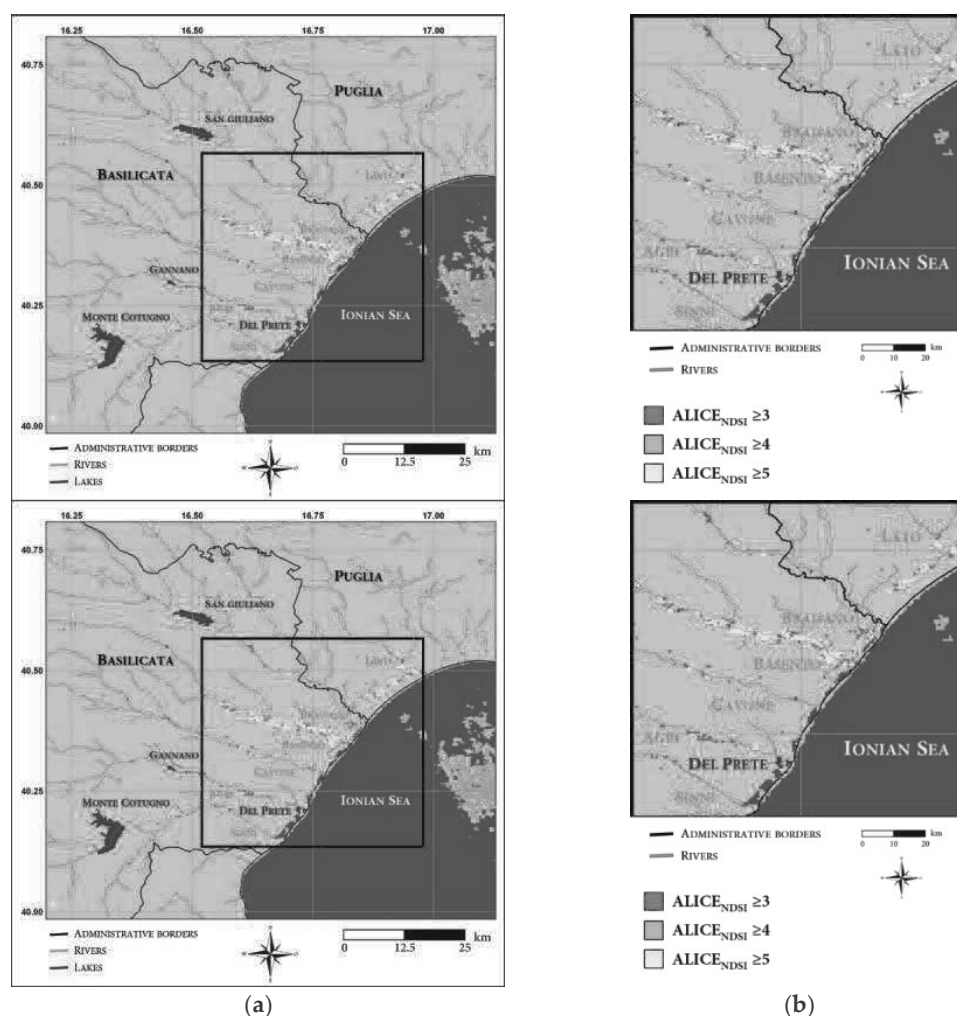

(a) (b)

Figure 9. (**a**) Flooded areas detected within the ROI by ALICE$_{NDSI}$ on 04/12/2013 at 12:10 GMT at increasing levels of the confidence from red to yellow; (**b**) magnification of the area within the white box shown in Figure 1.

Once the most suitable ALICE index has been defined, it has been applied also on the next four days (i.e., up to 8 December 2013), when the event should have been already ended, according to previous works (e.g., [31,37]).

The map including all the anomalous pixels detected by the ALICE$_{NDSI}$ $\geq$ 3 during the five days is reported in Figure 10, clearly showing as the probably effects of the event were still evident up to 8 December at least. In the following days, the ROI was again cloudy up to 10 December 2013, when the flood effects were almost disappeared. The spatial extent of the detected anomalies during the five-day period was about 72 km^2 on December 4th, 41 km^2 on 5th, 32 km^2 on 6th, 38 km^2 on 7th and 30 km^2 on 8th December 2013, respectively. A clear decreasing trend in the anomalous area identification is notable (as expected in the case of floods), except for 7th December, when the large presence of clouds and relatively shadows may have produced a few false positives (see green pixels in Figure 10). Moreover, the clusters of anomalous pixels in correspondence of the main affected rivers as well as their persistence in the spatiotemporal domain, suggest their possible direct correlation with the flooded area that will be assessed in the next session.
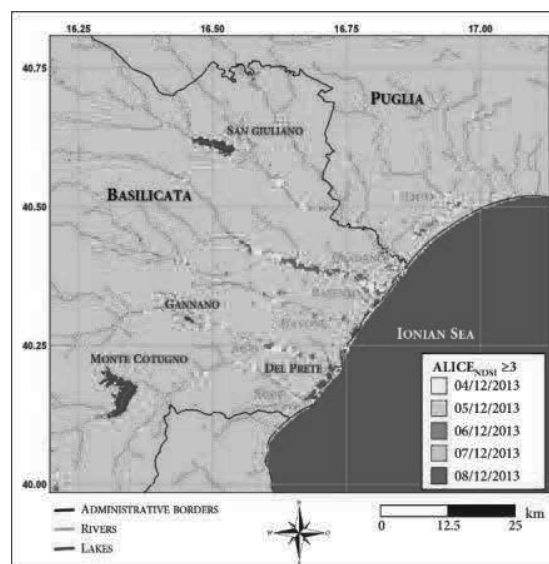

Figure 10. Flooded areas detected within the ROI by ALICE$_{NDSI}$$\geq$3 on days between 4–8 December 2013.

4.3. Assessment Results

4.3.1. Comparison with Landsat 7 ETM+ Data

The RST-FLOOD results referring to 5 December 2013 were superimposed on the water affected areas shown in Figure 3c in order to assess their reliability. By comparing the areas detected as flooded by RST-FLOOD (orange pixels in Figure 10) and the change detection scheme, described in Section 3.2, on Landsat 7 ETM+ data (Figure 3c), a very good level of agreement can be observed (Figure 11).

Across the scene, 191 and 357 pixels were flagged as flooded in the Landsat and RST-FLOOD map, respectively, with 120 common detections (Figure 11a). The remaining Landsat water affected pixels, not detected by RST-FLOOD, are around the lakes/dams (35%) and along Basento and Bradano rivers (65%). Within the box (Figure 11b), ~90% of total pixels detected by Landsat (i.e., 104) are also identified by RST-FLOOD that found a total of 293 pixels. Those remaining are all along the Basento and Agri rivers and were not detected by Landsat due the already-mentioned data gap acquisition.
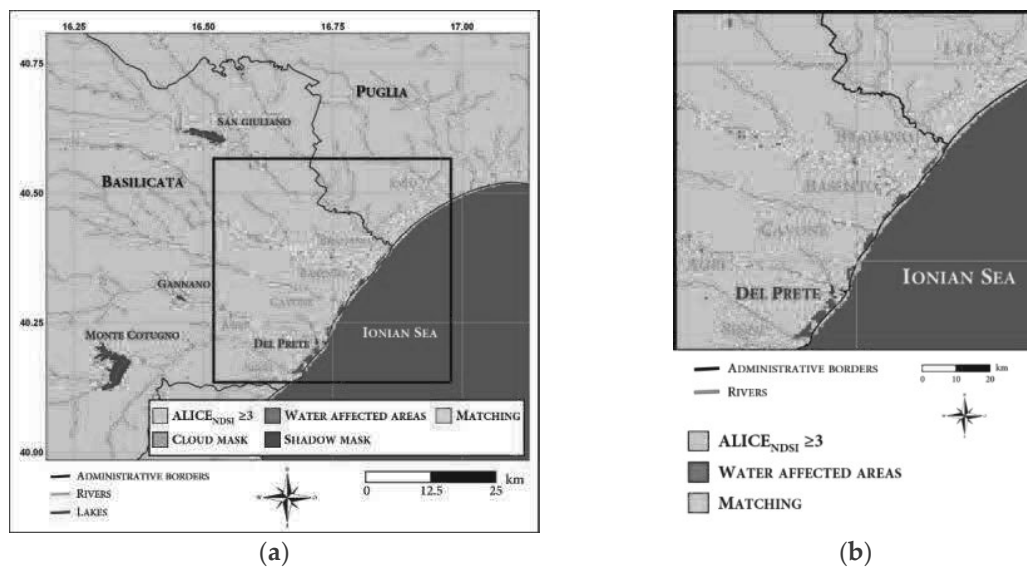
Figure 11. (**a**) Comparison between the flooded affected areas detected by RST-FLOOD for the 5 December 2013 (orange pixels) and the water affected areas computed by a change detection scheme on Landsat data (magenta pixels); the common pixels are highlighted in green; (**b**) a magnified map of (**a**) within the white box shown in Figure 1.

4.3.2. Comparison with the Flood Risk Map

The flood hazard map (Figure 4) provided by the Italian Ministry of the Environment and Land Protection was used to assess the reliability of the proposed approach. All the ALICE$_{NDSI}$ anomalous pixels detected by RST-FLOOD in the 4–8 December 2013 temporal range have been superimposed on the PAI area (Figure 12).
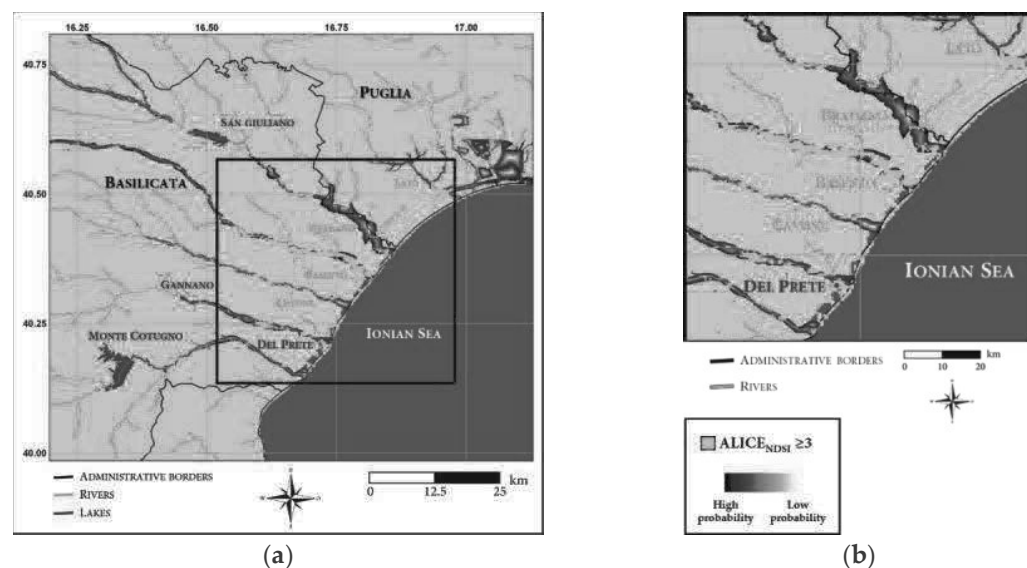

Figure 12. (**a**) PAI and anomalous pixels detected by RST-FLOOD (ALICE$_{NDSI} \geq 3$) in 4-8 December 2013 over the ROI; (**b**) a magnified map of (**a**) within the white box shown in Figure 1.

Table 3 summarizes the amount of anomalous pixels falling or not within the PAI area, counted considering both the whole scene and the above-mentioned black box (shown in Figure 12b).